UCP Journal of Science and Technology
Vol. 1, Issue 2 (January – June 2024)
Journal website: http://ojs.ucp.edu.pk/index.php/ucpjst/index

Numerical Modelling and Rugged Techniques for De-orbiting of LEO Space Debris

Ghulam Jaffer[1]*, Khadija Shabir[2], Rameez Ahmed Malik[3], Farhat Iqbal[4], Muhammad Tahir Mushtaq[5] and Hafiz Adnan Ashraf[6]

Abstract

According to the statistics of Space Surveillance Network (SSN), approximately 200 on-orbit and 54 strident events occurred which smashed the debris into smaller segments. It is essentially needed to detect deliberated hypervelocity impacts, accidental collision between satellite and explosion of satellites that can form potential a debris cloud. Space debris constitutes failed spacecrafts and upper stages of rockets etc.) occupies substantial space at all the altitudes of LEO, MEO and GEO, which may pose a threat to operational and future missions. There are multiple techniques to mitigate the threatening space debris via targeted deterrent measures, such as passivation measure or active de-orbiting. This paper presents a numerical modeling technique for identification of debris clusters based on density distribution, A/m ratio and explosion velocity. The breakup events of Fengyun-1C, NOAA-16, Iridium 33 and Cosmos 2251 have been considered for dynamic analysis on the basis of real-time orbital data. The debris population is presented in term of their classical orbital elements using statistical tools. A rugged technique is devised for the removal of millimeter and centimeter level debris fragments. It is a cost-efficient yet effective approach, implemented with aid of a Hoover Capturing System (HCS). This system is composed of a current carrying conductor which produces a magnetic field similar to that of a bar magnet. The target fragments would be captured by HCS on close approach of the system. Afterwards, HCS would be transported to a low parking orbit where it would dispose of the junk through a suitable window of opportunity. Ultimately, fragments would be burnt on reentry into lower altitude by atmospheric drag. This technique is very rugged, cost-efficient and can be utilized for frequent cycles.

Keywords: Debris, Active Debris Removal (ADR), Hoover Capturing System (HCS), Atmospheric Drag, and De-Orbiting

[1]Interdisciplinary Centre for Security, Reliability and Trust (SnT), University of Luxembourg, Luxembourg
[2]Mechanical Engineering and Mechanics Department, Lehigh University, Bethlehem, PA, USA
[3]School of Mechanical and Manufacturing Engineering, University of New South Wales (UNSW), Sydney, Australia
[4]Research Associate Department of Electrical and Computer Engineering, TU Berlin, Germany
[5]SST, University of Management and Technology (UMT), Lahore, Pakistan
[6]School of Astronautics, Beihang University of Aeronautics and Astronautics, Beijing, China
*Corresponding author's E-mail: ghulam.jaffer@ieee.org
Article History:
Received:10-12-2024; Received in revised form: 21-01-2024; Accepted: 23-01-2024
Available online: 01-04-2024

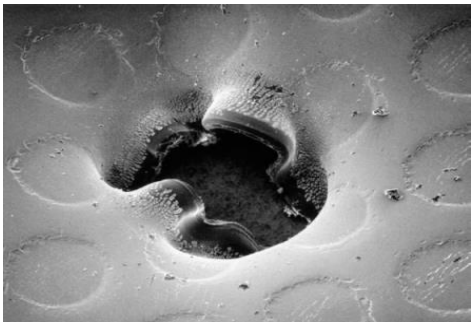

Figure 1 3mm paint flake damage the spacecraft (Stansbery 2009).

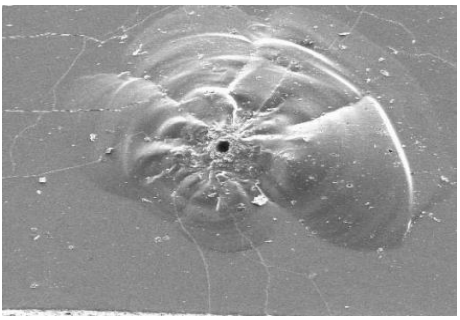

Figure 2 0.1mm Aluminum debris damage the window of the spacecraft (Stansbery 2009).

1. Introduction

Space debris is a form of unavoidable space junk being produced by high demanding space missions. There have been more than 630 events which include break ups, explosions, collisions and uncharacteristic events resulting in fragmentation (Figure 1 and 2). It is evident from the literature that about 500,000 debris pieces larger in size of 1 cm are present (Lemaître, 2019). Similarly, about 135,000,000 greater than 1 mm, over 300,000 fragments greater than 10 cm and fragments up to 1m or greater have been tracked in LEO (400- 2000 km), MEO (2000-36000 km) and GEO (36000 km), orbiting at a velocity of several kms^{-1} (Stansbery 2014). Most of the debris is produced as result of space activities of major space actors like United States, Russia, China, and Europe etc. The operational satellites and debris have been monitored by the Air Force Space Command (AFSPC) with aid of 25 tracking Radars and optical telescopes. As Radar is not powerful enough to penetrate the altitude above several hundred kilometers; consequently, the optical sensors are of critical importance in debris surveillance and archiving (Klima, Bloembergen, Savani, Tuyls, Hennes, & Izzo 2016), (Hamilton, Blackwell, McSheehy, Juarez & Anz-Meador, 2017).

According to United States Strategic Command (USSTRATCOM), since the launch of first artificial satellite (Sputnik-I), there are about 300,000 debris particles have been tracked in LEO (Maxwell, 2009). The diameter of these particles is greater than 10 cm with approximate mass of 1kg. Space Surveillance Network (SSN) tracks about 31630 objects on a regular basis and catalogues these objects as Two-Line-Element (TLE) (Stottler, 2015). It is estimated that particles less than 10 cm are untraceable due to the sensor's sensitivity constraint. Nowadays, space debris is major threat to continuously increasing space activities and new missions as well. The collisions with operational satellites cannot be prevented at the time of trajectory corrective maneuvers due to the presence of these small debris. The distribution of debris varies in LEO, MEO and GEO due to the high solar drag; however, most of their fragments are found in LEO at 800-850 km altitude due to high concentration of SSO satellites for Earth imaging and communication satellites in polar orbits (Silha, Schildknecht, Hinze, Utzmann, Wagner, Willemsen & Flohrer, 2014).

The space objects are classified as payloads (functional satellites), rocket bodies, debris fragmentation and unknown debris at various orbital altitudes. Due to the incredible buildup of space debris, it is a challenging job for NASA to figure out this entire debris in space (Liou 2011). Therefore, NASA dedicates a latest 1.3 m optical Meter Class Autonomous Telescope (MCAT). The MCAT is deployed at Johnson Space Center, Orbital Debris Program Office (JSCODPO) with four primary operational modes. It can precisely produce and process excess data

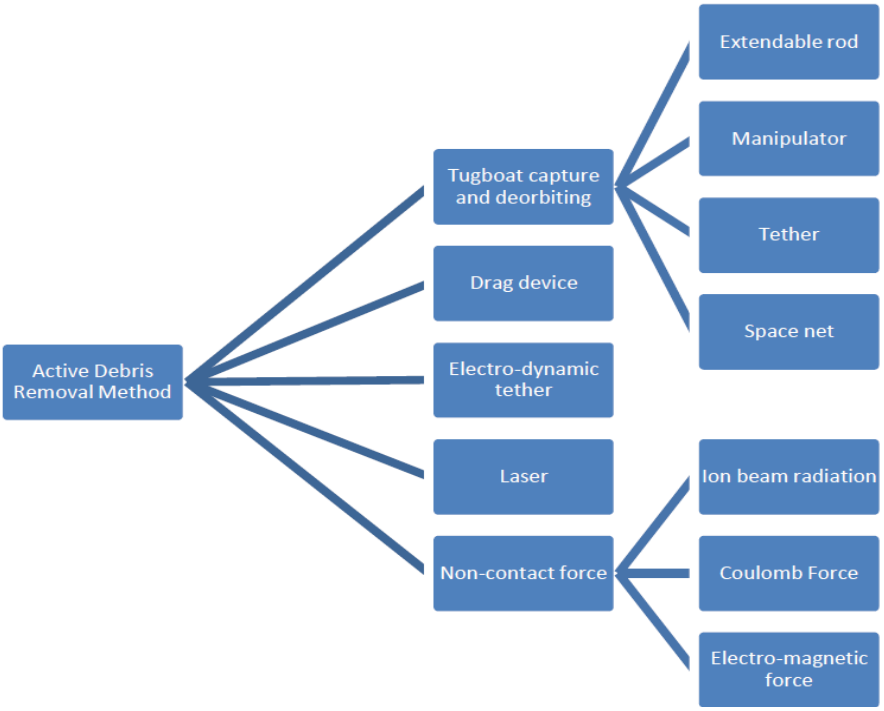

Figure 3 Active debris removal methods

volumes with astrometry and automated re-acquisition (Lederer, Stansbery, Cowardin, Hickson, Pace, Abercromby, & Alliss, 2013).

As it is well established fact that debris is a high potential risk for space activities. Therefore, aim of this paper is to investigate the numerical modeling techniques for debris location and identification. It also discusses Active Debris Removal (ADR) technique for small fragments (less than or equal to 10 cm) depicted in Figure 3. The structure and design of ADR system is discussed in detail and the paper is divided into following sections: Section 2 describes the physical properties of debris fragments, i.e. density and Area to mass (A/m) ratio of debris objects. The size, A/m ratio and expulsion velocity of all the debris fragment is not same due to difference in their physical properties and altitude levels.

The orbital position of debris in terms of keplarian orbital elements (semi-major axis, eccentricity, inclination, RAAN, mean anomaly), velocity distribution and uncertainty associated with position and velocity in explained section 3. The uncertainty in position and velocity is caused by various factors that influence the motion of objects in orbit. These factors include drag of the atmosphere, gravitational effect due to geopotential, solar and lunar forces and Solar Radiation Pressure (SRP). Section 4 and 5 explains de-orbiting technique for debris removal and design/specifications of the service platform. There are various methods which are currently being under analysis for ADR. These methods are illustrated in Figure 3 (Liou, 2011), (Rezunkov, 2013). The ADR method, is compelled with multiple limitations and works under several assumptions such as technological constraints may impact the efficiency with a finite range, potentially restricting its effectiveness at orbital ranges. High resource and energy requirements could limit to conduct multiple removal missions simultaneously. Finally, mission duration and End of Life (EOL) also pose challenge

Table 1 Magnetic properties of materials

Material	Magnetic ordering	Magnetic susceptibility, cm^3mol^{-1}	Density, gcm^{-3}
Aluminum	Paramagnetic	$+16.5 \cdot 10^{-6}$	2.70
Titanium	Paramagnetic	$+153.0 \cdot 10^{-6}$	4.506
Nickel	Ferromagnetic	-	8.9

to stand out in a cluttered orbital environment.

2. Physical properties of debris

Nowadays, lightweight materials have been adopted as a standard in aerospace industry for design and development of spacecrafts. The main advantage of lightweight materials is the reduction of spacecrafts dry mass to lessen mission launch cost. However, highly dense and materials are mostly used in manufacturing of a spacecraft. Desired strength is attained with high efficiency structural materials (aluminum and titanium etc.) at normal temperatures. Meanwhile, nickel and ferrous alloys are mostly optimum for extreme thermal environment materials as these are the best high temperature metals. Iron is a ferromagnetic material and its alloys also demonstrate magnetic properties. A material whose value of density is greater than zero, that kind of substance is known as paramagnetic. The magnetization of a paramagnetic material is higher than that of free space. On the other hand, the substance is diamagnetic if its density is less than zero (Deshpande, Green & Zarnecki, 1993). The magnetic properties of materials are depicted in Table 1.

The collision and explosion events that have been analyzed in this paper are discussed as follows:

Fengyun-1C: This satellite had undergone a hypervelocity projectile impact on January 11, 2007. The mass of this satellite was approximately 880 kg. As a result of this impact, almost 2000 fragments bigger than 5 cm and 1000 fragments bigger than 10 cm that have been cataloged SSN. Most of these fragments are present at LEO altitudes in high concentration (Pardini & Anselmo, 2011).

Cosmos 2251 and Iridium 33 Collision: In 2009, these satellites suffered a collision which caused Cosmos 2251 to generate 1669 fragments and Iridium 33 to produce 627 fragments (Pardini & Anselmo, 2011).

Explosion of NOAA 16: It was a meteorological satellite, launched in Sun Synchronous Orbit (SSO) at an orbital height of about 850 km. It undergone break up because of battery explosion on November 25, 2015. Almost 400 pieces greater than 10 cm have been catalogued, though it produced an unknown amount of tiny un-trackable debris. There are only 53 fragments which have been catalogued on 5 December 2015. The NOAA 16 has produced maximum number of high-density fragments (steel) and other solid fragments of low-density material. The remaining debris is considered to be formed of moderate density materials, i.e. aluminum or solid electronics. A very small amount of low-density material is present in NOAA-16 cloud. The analysis reveals that fragmentation event of this satellite consisted of only 2% (36kg) of the total satellite dry mass (Tan, Reynolds & Schamschula, 2017). If we consider some expected discrepancies because of structure and energy, we can compute the quantity of blasted pieces having size of equal of greater than 1m using expression below (Wang, 2010):

$$N(L_c) = 6L_c^{-1.6} \quad (1)$$

Where, N is the number of exploded fragments and Lc is the fragment size.

2.1 Density distribution of debris fragmentation

The density distribution of debris fragment is mainly dependent on its material properties. In our analysis, we have considered that the fragments are composed of same material and therefore have density within the range of 1500 kgm^{-3} to 9000 kgm^{-3}. One the other hand, a honeycomb structured fragment might have approximately 150 kgm^{-3} of density. Moreover, there exists a relationship between density and A/m ratio of the fragmentation. Materials with high density like titanium, some aluminum alloys and steel occupy a low value of A/m ratio (approximately 0.001 - 0.1 $m^2\ kg^{-1}$). Conversely, low density materials like Multi Layer Insulation have high levels of A/m ratio (1 – 10 $m^2\ kg^{-1}$) (Sorge, Peterson & McVey, 2017), (Johnson, Krisko, Liou & Anz-Meador, 2001).

The characteristic density of fragment under analysis is determined with an assumption that it is spherical in nature. The mathematical equation that well represents the fragment density is given as follows: (Wang, 2010):

$$\rho_c(d) = 92.937(d)^{-0.74}\ (kg/m^3) \quad (2)$$

Where, ρc is the debris characteristic density and d is the diameter of debris fragment.

2.2 Size and A/m ratio distribution of debris fragmentation

The debris region / cloud formed by on-orbit impact and explosion is modeled by JSCODPO since 1970. This debris modeling is based on the physical properties of size and velocity distribution. We have utilized three methods, which we think are responsible for producing fragments. The data has been analyzed to determine their mass distribution (Bess, 1975).

a. Hypervelocity (3.0 - 4.5 kms^{-1}) projectile impact with satellite wall.
b. Explosion of high Intensity.
c. Explosion of low Intensity.

It must be noted that the quantity of fragments produced by hypervelocity impact projectile obeys power law. On the other hand, fragments formed from the explosions of high intensity and low intensity obey exponential law. It has been studied that the fragments produced due to hypervelocity projectile has mass up to to 10^{-7} grams and the mass of the fragments produced fragment produced due to explosion is 10 milligrams. Meanwhile, the velocity of fragments formed due to hypervelocity impact is 10 ms^{-1}. On the other hand, velocity of the fragments produced due to low intensity and high intensity explosions is about 100 ms^{-1} and 3 kms^{-1}, respectively (Bess, 1975). The size limit for catalogued objects in LEO is approximately 10 cm. For statistical analysis, we have considered 1000 fragments of Fengyun-1C, Cosmos 2251, NOAA 16 and Iridium 33 produced in various events.

A/m ratio of fragment is defined by Ballistic coefficient and expressed as a product of A/m ratio (cross section) and drag coefficient with the following equation (Hakima, Bazzocchi & Almstrom, 2022):

$$B = D_c \frac{A}{m}\ (m^2/kg) \quad (3)$$

Where, B Ballistic coefficient, Dc is drag coefficient and A/m is Area to mass ratio (cross-sectional). The parameter B is computed by SGP 4 spacecraft orbit propagation model (Hoots & Roehrich, 1980). We can estimate the cross-sectional area from Radar Cross Section (RCS), as this data is not given in Satellite Situation Report (SSR). Therefore, system description is acquired from Space-Track (RCS Legend, 2021). The parameter B is calculated from B-STAR parameter, as mentioned in Two Line Element (TLE) for the entire catalogued objects (CelesTrack, 2023). B-STAR actually provides the magnitude of atmospheric drag on an object (debris in our case). It is mathematically written as:

$$B^* = \frac{\rho_0 B}{2} \quad (4)$$

$$B^* = \frac{D_c \rho_o A}{2m} \quad (5)$$

Where B^* is B-STAR, its unit is inverse of earth radii (Earth $Radii^{-1}$). Further details of B* and TLE can be

obtained from CASTOR (Satellite Tracking and Optical Research, 2020); ρo represents atmospheric density. It has a value of 0.1570 kg Earth Radii m^{-2}. If we consider D_c = 2.2, The value of B* is obtained from TLE which allows us to estimate A/m ratio. By re arranging the equation (5), we may get (Satellite Tracking and Optical Research, 2020):

$$\frac{A}{m} = \frac{2B^*}{\rho_o D_c} \quad (6)$$

After determining the number of fragments from each sample (cluster), we may obtain a distribution of the sum of debris pieces having mass equal to or greater than a specific quantity. The A/m ratio of pieces has a direct link to orbital life/decay rate which means that higher A/m ratio results in smaller orbital life.

3. Collisions estimation and modeling of debris fragmentation

To determine the effect of collision, we need to find the ratio of relative kinetic energy of the object with small mass to that of large mass object. It gives the idea that the collision was catastrophic or not. This ratio of large mass object to small mass object gives us the information whether the collision was appalling or non- appalling. If this ratio is $\geq 40 Jg^{-1}$ then it is an appalling collision or otherwise it would be a non-appalling collision. When it comes to the phenomena of the number of fragments produced, power law is applied to a hypervelocity collision. An optimum estimation of cumulative number of fragments in terms of size (Lc) can be well established by NASA Breakup Model (EVOLVE 4.0). The mathematical expression for size estimation may be written as (Johnson, Krisko, Liou & Anz-Meador, 2001):

$$N(L_c) = 0.1(M)^{0.75} L_c^{-1.71} \quad (7)$$

Where Lc is fragment size (meters), M is the combined mass of both objects (kg). In case of catastrophic collision, the expression may be written as:

$$M' = m_L + m_s \quad (8)$$

Incorporating the value of M, the Equation (6) may be written as:

$$N(L_c) = 0.1(m_L + m_s)^{0.75} L_c^{-1.71} \quad (9)$$

Where, mL is mass of larger object and mS is mass of smaller object. On the other hand, if the collision is non-catastrophic, M is the product mass of small body (kg) and collision speed (kms^{-1})

$$M = m_s \times v_c \quad (10)$$

In this case, equation (7) may be represented as:

$$N(L_c) = 0.1(m_s v_c)^{0.75} L_c^{-1.71} \quad (11)$$

The dry mass of cosmos 2251 was 900 kg and that of Iridium 33 was 556 kg. The collision of these satellites took place at 770 km altitude. The Iridium 33 was an operational communication satellite and cosmos 2251 was debris at the time of impact. Both satellites were orbiting the globe with velocity of 7.5 kms-1and collided with over 10 kms-1 velocity. The debris produced because of this collision was within range of massive objects to dust particles. Iridium produced about 550 fragments of iridium and 1,300 fragments of cosmos were produced that were larger than 10 cm diameter. According to NASA Breakup Model, cosmos 2251 produced 840 fragments larger than 10 cm, 43220 pieces larger than 1cm and 2.22e6 fragments greater than 1mm. The iridium 33 generated 580 fragments bigger than 10 cm, 30 fragments larger than 1cm and 100 fragments larger than and 1.54e6 (Wang, 2010). Iridium 33 fragments has higher A/m as compared to Cosmos 2251, which would decay in a short life span. The reason for high A/m ratio of iridium is correlated with the structural composition of its two solar panels.

As we know, RCS gives the size approximation of the debris pieces and is not suitable for the estimation of fragments less than 10 cm. Ting Wang model is adopted for the estimation of size distribution of iridium-cosmos cloud. This model presents an effective valuation of fragment size to their cumulative number. The size distribution of Iridium and Cosmos shows that most of the fragments are larger than 10 cm in size (Wang, 2010). Table 2 shows the physical properties of

Table 2 Physical properties of Cosmos 2251, Iridium 33, and Fengyun 1C from NASA breakup modell

NORAD ID	Name	A/m m^2kg^{-1}	RCS, m^2	m_s kg	N_c>10 cm
34333	Cosmos2251	0.00395	0.0354	0.2224	25
34398	Cosmos2251	0.00383	0.0317	0.2561	41
34657	Iridium 33	0.01430	0.0136	0.0403	8
34858	Cosmos2251	0.07307	0.0137	0.0509	13
30455	Fengyun 1C	0.00287	0.0282	0.7377	113
30687	Fengyun 1C	0.01038	0.0195	0.0740	29
30980	Fengyun 1C	0.00724	0.0127	0.0486	26
31998	Fengyun 1C	0.01006	0.0118	0.0428	23
36697	Fengyun 1C	0.00048	0.0093	0.2787	88

the fragments created from the collision. These calculations are based on NASA Breakup Model. Because of the tracking constraint of SSN radar, only objects of 10 cm or larger size can be measured.

In case of Fengyun-1C, the size and A/m ratio distribution is unique from other identical events. About half of the pieces are made of light material and above hundred fragments have A/m greater than 1 m^2 Kg^{-1}. These fragments constitute the pieces of spacecraft's thermal insulation and solar panel. If we apply NASA model, we conclude that satellite with a mass of 960 kg would generate more than 900 fragments which are less than 10 cm in size (Pardini & Anselmo, 2007). The cumulative size distribution of Fungyun-1C fragments is below 13 cm. This is because of the lack of sensitivity of the SSN sensors to tiny fragments. The Haystack Radar measurements further reveal that Fengyun-1C has created unusual quantity of fragments as compared to other similar and average hypervelocity. The size distribution of Fengyun-1C size shows deviates from single power law distribution. There is another prominent property associated with the Fengyun-1C fragments is the high A/m ratio (0.1 m^2kg^{-1} and higher). The Fengyun-1C spacecraft was composed of two solar panels having a dimension of 1.5 m × 4 m. Each of the solar panels was insulated with 13 m^2 Multi-Layer Insulation (MLI). It is thought that high A/m ratio fragments are resulted from the breakup of solar panels, MLI and light weight plastic material etc. (Liou, J & Johnson, 2009).

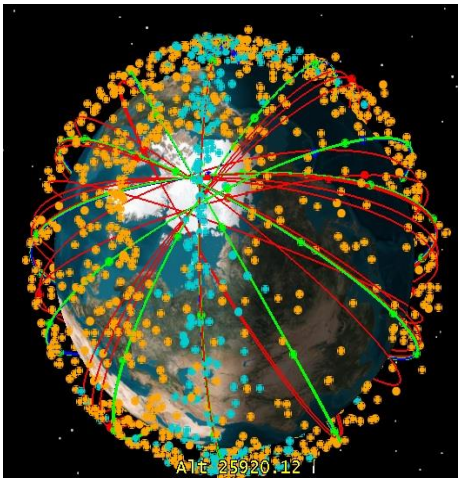

Figure 4 Visualization of orbits of Cosmos 2251 and Iridium 33 debris fragmentation.

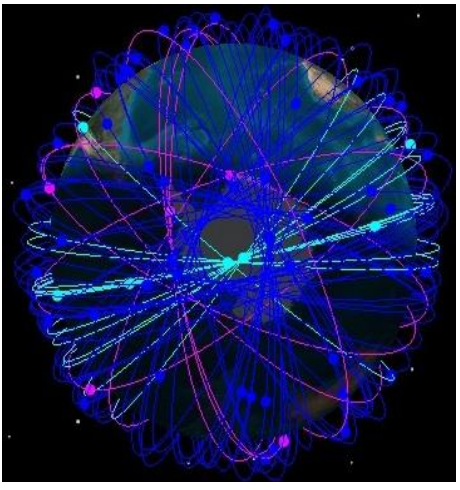

Figure 5 Visualization of orbits of Fengyun 1C debris fragmentation.

4. Simulation and statistical analysis of debris fragmentation in terms of keplarian elements

The simulation analysis has been performed with the help of dynamic simulator. The orbits are propagated on SGP 4 propagator on the basis of TLE data (CelesTrack, 2023). Approximately 1000 files of the orbital data of Fengyun-1C, Cosmos 2251, Iridium 33 and NOAA 16 have been incorporated in the simulator as shown in Figure 4 and 5 to analyze debris population of Fengyun 1C, NOAA-16, Cosmos 2251 and Iridium 33 in term of their orbital elements (semi-major axis, inclination, RAAN, eccentricity, argument of perigee and mean anomaly). The results of simulation analysis are represented in graphical form in Figure 7 to 10.

The most important distribution is

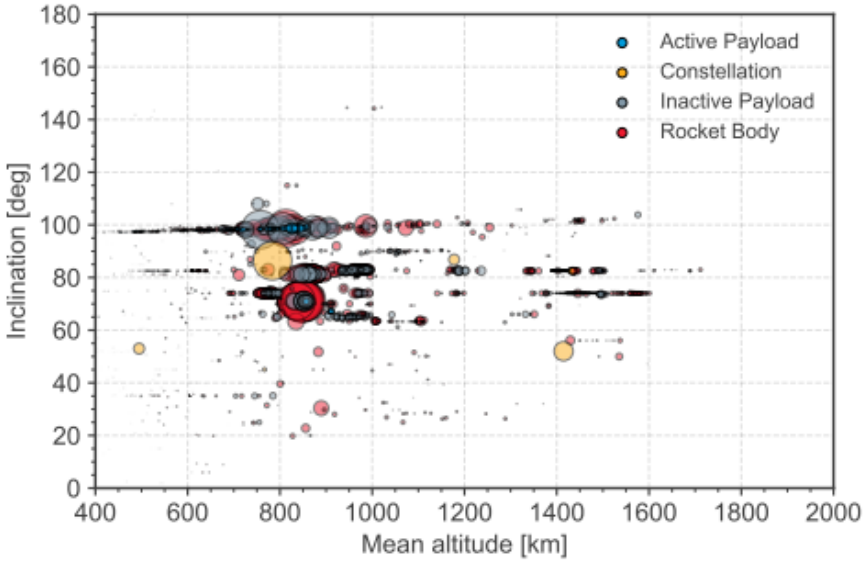

Figure 6 Debris cataloged by ESA (Annual Space Environment Report 2022) at multiple altitudes and inclination angles, courtesy ESA (ESA, 2022).

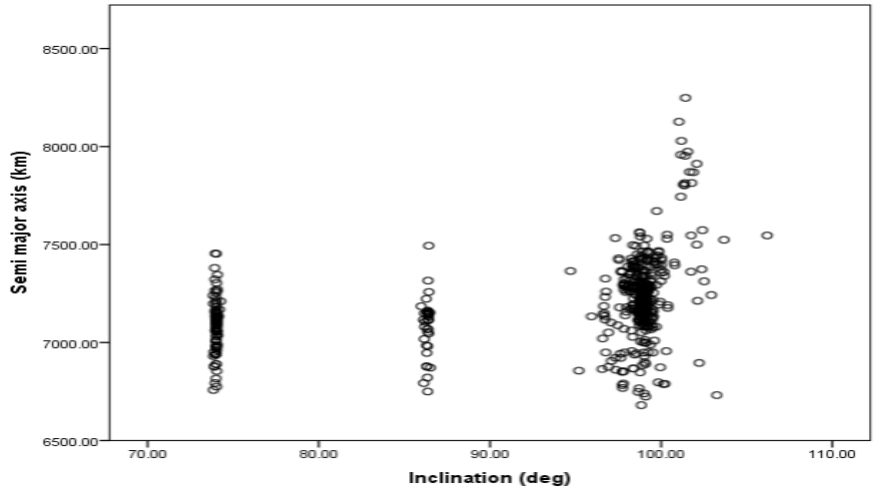

Figure 7 Representation of debris distribution as a function of inclination and semi major axis.

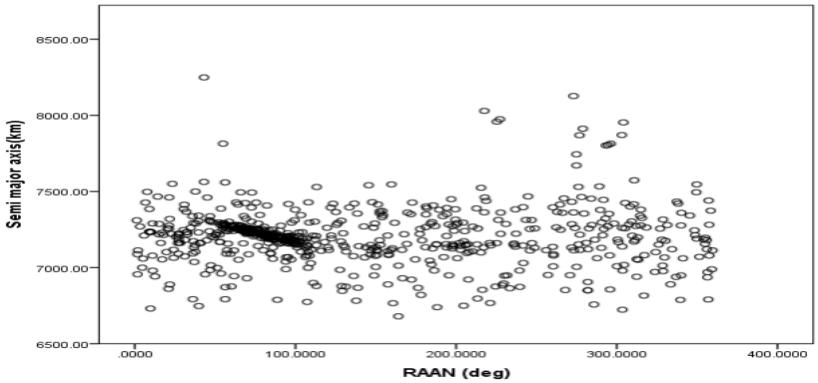

Figure 8 Representation of debris distribution as a function of RAAN and semi major axis.

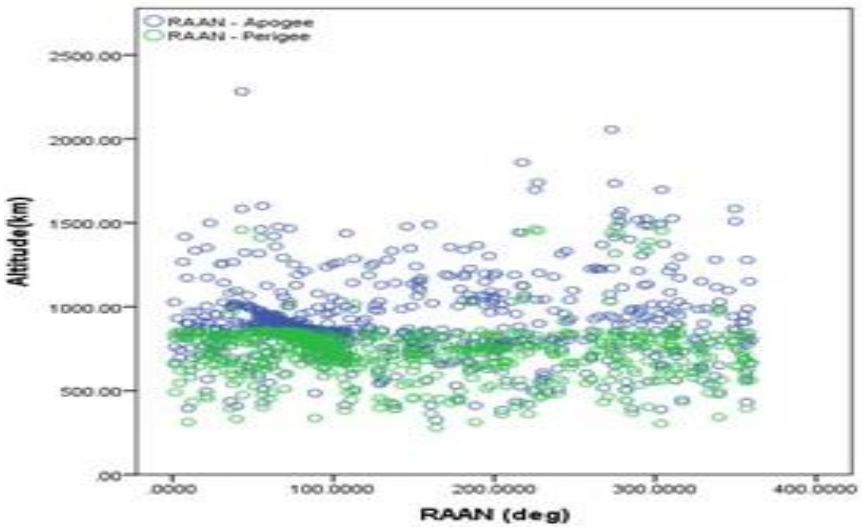

Figure 9 Representation of debris distribution as a function of RAAN, perigee altitude and apogee altitude.

depicted in Figure 5 which identifies the debris concentrated areas as a function of inclination and semi-major axis (altitude). The plot reveals that fragments are concentrated on semi major axis of range between 6800 and 8000 km which correspond to altitude range of 422 km and 1622 km at an inclination close to 1000. The distributions also reveal a fact that debris from various events (collision or explosion) formulate into clusters. Consequently, the ADR task from numerous fragmentation events becomes feasible and convenient with a single mission design and operation.

There is another orbital parameter along with inclination which defines the orientation of an orbit. This orbital parameter is RAAN. RAAN and semi-major axis distribution is also of critical importance to precisely locate the debris cluster. This distribution is presented in Figure 9 which shows that most of the debris is concentrated within RAAN bin of 50.8 o to 94.6 o corresponding to the semi-major axis range of 6800 and 8000 km. The debris cluster within this range of altitude and RAAN is extremely suitable for the ADR. The critical regions with debris cluster in terms of altitude and inclination are 850 km and 71º, 1000 km and 82º and 800 km and 98º respectively, corresponding to RAAN bin of 50.8 o to 94.6 o. It must be noted that for a single

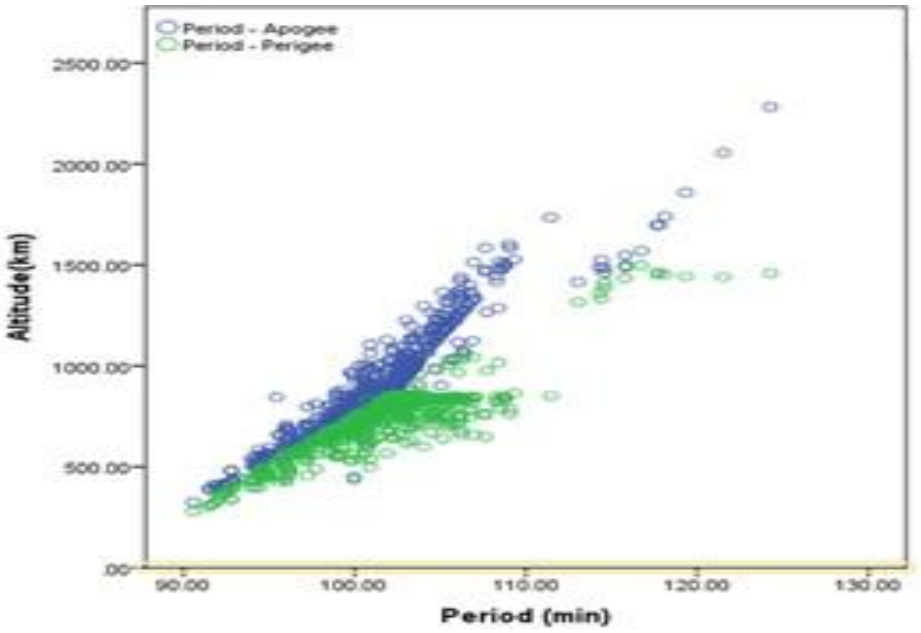

Figure 10 Representation of debris distribution as a function of orbital period, perigee altitude and apogee altitude.

inclination, position of the fragments is different in each bin of RAAN, we may have to perform multiple rendezvous attempts in a single operation.

The European Space Agency (ESA) has cataloged debris real data (figure 6) at multiple locations which can be correlated to current study (ESA, 2022).

The plot of apogee and perigee altitude against RAAN of debris fragments under against RAAN of debris fragment under analysis is given in Figure 9. This plot also shows that the junk concentrated region lies within RAAN bin of 50.8^{o} to 94.6^{o} corresponding to the altitude of range of 622 and 1122 km. The distribution of fragment apogee and perigee altitude as a function of orbital period is depicted in Figure 10. The overall results of the simulation analysis establish the fact Keplarian elements make it easy to identify the position of the space debris in terms of semi-major axis, inclination and RAAN. However, it must be noted that there are some uncertainties due to the perturbation effects. The magnitude of these uncertainties can be managed with high update rate of orbital data in the simulation.

5. Active Debris Removal (ADR) technique

After debris identification, further aim of this paper is to propose cost-efficient debris removal algorithm. The idea is to capture and safely remove debris within the identified fragments from the selected altitude regions. It would be done with a servicing platform, composed of numerous stages. The primary component of this platform would be a Hoover System (HS) and secondary supporting equipment include the Hybrid Rocket Motor (HRM) to perform de-orbiting operation, propulsion system to perform rendezvous maneuver and maintain attitude and communication system for telemetry and command of the space mission (Carmicino & Sorge, 2007). The whole idea is that once the platform approaches the targeted fragments; they would be captured by HS. It would produce electromagnetic attraction force with the help of large solenoids. The whole concept of ADR is discussed in detail as follows:

5.1 Rendezvous phase The rendezvous phase begins with maneuvering of servicing platform already inserted and parked in the target (fragment cloud)

orbital plane. The rendezvous phase is subdivided into various stages, discussed as follows:

Phasing with the target: To start rendezvous, various orbital phase changing maneuvers have to be performed to transfer the service platform from parking orbit to targeted debris cluster. These plane-change orbital maneuvers are based on Hohman transfer technique as it is an efficient and energy saving technique. Figure 11 demonstrates the orbit transfers required to first approach, rendezvous, capture and transfer the debris fragmentation to low altitude for re-entry. When the platform reaches the phasing orbit, distance between service platform and debris cluster (target) would decrease to few kms. There can be some uncertainty in cluster location because of the limited accuracy of orbital data (ground track and TLE). The precise position of the target cluster would be achieved with the help of onboard optical sensors like far range camera or star sensor and infrared sensor during of eclipse. Line of Sight (LOS) of the cluster is one of the most critical types of information which would be obtained from a far range sensor to carry out the phasing maneuvers accurately. Similarly, camera imagery combined with GPS receiver data would provide parameters of range and range rate to establish relative movement of the platform with respect to the target. The initial optimum identification of the target would be acquired from optical sensor. Moreover, the time when relative distance between the platform and cluster reduces from kilometer to meter level, near range rendezvous phase would be initiated with the aid of a near range camera and monocular or stereo-vision methods.

Mid far range rendezvous: When the server platform approaches near target, a mid-far range rendezvous is needed to bring the servicing platform near to the cluster. To carry out this rendezvous, technical equipment must be precise to avoid any serious issue in this operation. Technologically verified equipment could be acquired from other similar rendezvous operations, e.g., DEOS mission, RRM mission and Phoenix Program of NASA.

Close range rendezvous HCS: An identification and inspection with target fly

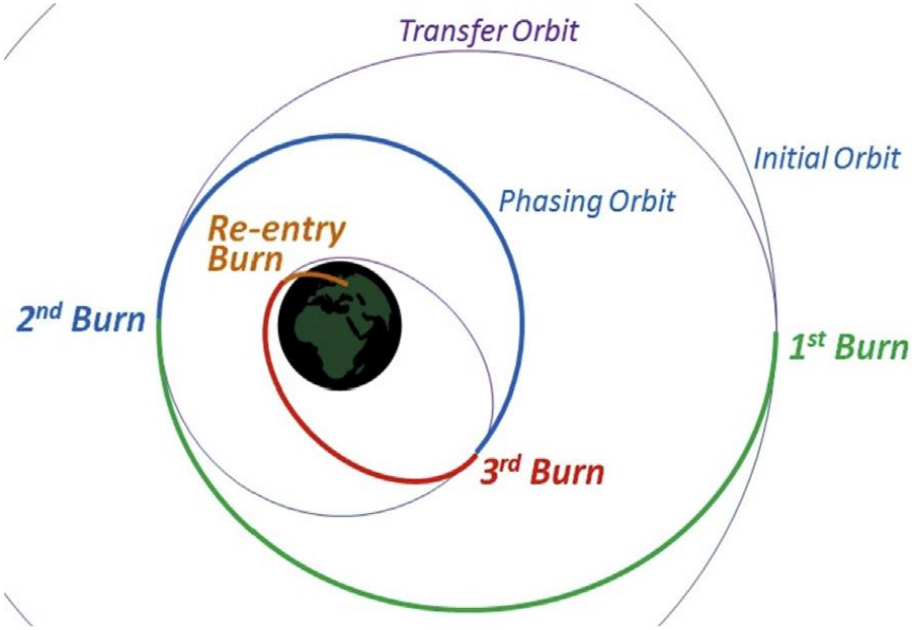

Figure 11 Illustration Hohmann technique for orbital transfers required for approach, rendezvous and transfer the debris cluster.

Table 3 Illustration rendezvous stages and detectors for identification and tracking of debris.

Stages	Maneuver	Sensor	Separation
Phasing	Target Phasing (absolute navigation)	GPS	~10 km
Far-mid range rendezvous	Tracking and prelude identification of the cluster (relative navigation)	Infrared or optical sensor of far-mid range	~10 m
Close range rendezvous	Fly around of HS for identification and inspection (close immediacy navigation)	Infrared or optical camera of close range	~1 m

around is needed before capturing the target. This action is necessary for the selection of the finest positions for capture maneuver. A close-range infrared/optical camera would be used for close range rendezvous phase. This phase is of critical importance because it is the final stage of rendezvous and the platform would start to capture the targets with the HCS. Therefore, major challenges would be mitigated with state-of-the-art technology and superior mission planning. This involves the determination of the critical parameters loke relative velocity, angular momentum and energy of the cluster. Meanwhile, synthetic information would also be acquired to compute the relative orientation of the cluster with respect to the platform. For this purpose, several algorithms can be utilized, such as, contour mapping, linearization and detection of edge. A brief description of various stages of rendezvous phase and detectors/sensors for identification and tracking of debris cluster is presented in Table 3.

We suggest a practically feasible methodology for the removal of 10 cm or larger fragments. It is named as Hoover Capture System (HCS) and its operating principle is similar to that of the vacuum cleaner. The only difference is that there is magnetic field instead of air that sucks up all the debris to be disposed of on a later stage. This HCS is a type of transducer, mainly composed of cylindrical solenoids, which are mounted with base of cylinder to generate magnetic field. The solenoid is basically composed of an insulated copper wire that is winded on a metallic core to produce uniform magnetic field. The general behavior of a solenoid is electromagnetic in case when a controlled magnetic field is needed. The power supplied to the solenoid would be generated by the solar panels. The left-hand side of the solenoid acts as south pole and right-hand side acts as north pole, if the current flow direction is clockwise and vice versa. The value of magnetic flux (B) can mathematically be presented by the Ampere law (Lim & Greenside, 2016):

$$B' = \mu_o \frac{NI}{l} \tag{12}$$

In the above equation, B' magnetic flux, N represents total turns in the coil, I is electric current, l solenoid's length and μ_o is the free space permeability. It must be noted that B has a direct relation to N, which implies that higher value of N would result in higher B. If we consider the case that the coil is wounded across a material with a permeability of μr, the increase in magnetic field can be expressed as:

$$B' = \mu_o \mu_r \frac{NI}{l} \tag{13}$$

An assumption is made that the current is evenly distributed over the surface of a fixed continuous solenoid. We may denote the radius of solenoid as a, length of solenoid as L and its current density with K. The value of B can be calculated using magnetic vector potential component A_φ in φ-direction, hence in cylindrical coordinates (ρ,φ,z) (Lim & Greenside, 2016) .

$$\vec{K} = \frac{I}{L}\hat{\varphi} \tag{14}$$

$$A_\varphi = \frac{\mu_o I}{4\pi}\frac{1}{L}\sqrt{\frac{a}{\rho}}\left[\beth k\left(\frac{k^2+H^2-k^2H^2}{k^2H^2}K(k^2) -\right.\right.$$

$$\frac{1}{k^2}E(k^2)+\frac{H^2-1}{H^2}\prod(H^2,k^2)\Big)\Big]_{ↄ_-}^{ↄ_+}, \quad (15)$$

Where,

$$ↄ_\pm = z \pm \frac{L}{2}$$

$$H^2 = \frac{4a\rho}{(a+\rho)^2}$$

$$k^2 = \frac{4a\rho}{(a+\rho)^2+ↄ^2}$$

$$K(m) = \int_0^{\pi/2} \frac{1}{\sqrt{1-m\sin^2\theta}}\,d\theta$$

$$E(m) = \oint_0^{\pi/2} \sqrt{1-m\sin^2\theta}\,d\theta$$

$$\prod(n,m) = \int_0^{\pi/2} \frac{1}{(1-n\sin^2\theta)\sqrt{1-m\sin^2\theta}}\,d\theta \quad (16)$$

In the above equations, last three expressions are complete elliptic integrals of equation 13, 14, and 15. As we know:

$$\vec{B} = \nabla \times \vec{A} \quad (17)$$

Thus magnetic flux density becomes

$$B_\rho = \frac{\mu_0 I}{4\pi}\frac{1}{L}\sqrt{\frac{a}{\rho}}\left[ↄk\left(\frac{k^2-2}{k}K(k^2)+\frac{2}{k}E(k^2)\right)\right] \quad (18)$$

$$B_z = -\frac{\mu_0 I}{4\pi}\frac{1}{2L}\frac{1}{\sqrt{a\rho}}\left[ↄk\left(K(k^2)+\frac{a-\rho}{a+\rho}\prod(h^2,k^2)\right)\right]_{ↄ_-}^{ↄ_+} \quad (19)$$

The radial component will be vanished on the symmetry axis, thus the axial field component is

$$B_z = \frac{\mu_0 NI}{2}\left(\frac{\frac{l}{2}-z}{l\sqrt{a^2+(\frac{l}{2}-z)^2}}+\frac{\frac{l}{2}+z}{l\sqrt{a^2+(\frac{l}{2}+z)^2}}\right) \quad (20)$$

As $(\frac{l}{2}- |z| \gg a)$ inside the solenoid far away from the end, the equation becomes $B = \frac{\mu_0 NI}{l}$

5.2 Debris capturing and de-orbiting phase

As mentioned earlier, relative position of the cluster would be calculated after close range rendezvous phase. It would be done with the help of near range sensor by utilizing monocular or stereo-vision methods. When the relative location of the target is determined, an adequate amount of magnetic field of the solenoid would become available to attract the small piece of space junk within the cluster. It must be noted that the solenoids should be tough enough to bear the impact of small fragments. Once the entire cluster has been cleared, the system would be powered off so that all the fragments may demagnetize and settle down.

5.3 Controlled re-entry phase

After successful rendezvous, now next phase of the operation would be initiated to bring the junk from its present location to predefined parking orbit at 250 km. This altitude would be achieved with the help of a plane change maneuver. Approximately 50 ms-1 energy in terms of velocity would be required to decrease the perigee altitude to 90 km. At this point, the fragments begin to re-enter the atmospheric where they would experience strong heat due to drag and ultimately burnt. The heat intensity is dependent on numerous parameters, e.g. initial velocity, flight path angle and ballistic coefficient etc. It is extremely tough to forecast the accurate re-entry location of the captured junk. This is due to almost 10% prediction uncertainty for the remaining lifetime (Patera & Ailor, 1998).

6. Hybrid Rocket Motor (HRM) for transfer/launch of service platform HCS

Hybrid Rocket Motor (HRM) a vehicle to carry the service platform near the debris cluster to initial ADR mission. It is an innovative system with some added advantages like thrust couture, stop-restart ability, enhanced safety systems and cost efficiency. Above all, it has operation capability in dual mode, such that, gas or solid oxidizer and solid-state fuel (DeLuca, Lavagna, Maggi, Tadini, Pardini, Anselmo & Viola, 2014).

6.1 Engine design

These days HRM is built with an innovative geometry in which a swirl injection is utilized. This arrangement produces a rotational speed at the surface and axial speed along the center. The main

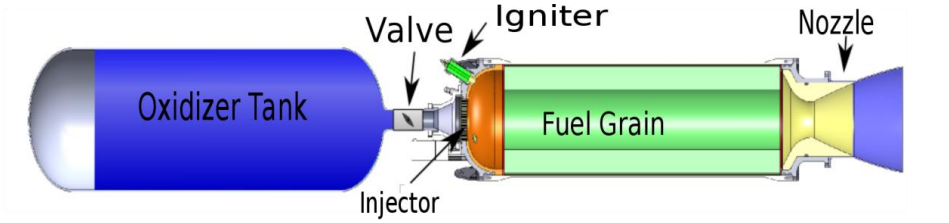

Figure 12 Fundamental deign of HRM

components include cylindrical solid fuel tank that is connected to the nozzle and oxidizer tank injector via ports. The oxidizer tank contains gas or liquid oxidizer material which flows towards the fuel tank via connected ports. This type of flow provides high stability during combustion process and is also critical for an optimum mixing of oxidizer with the fuel. In HRM, solid fuel is mixed with oxidizer within flame a zone flame. This flame zone is produced at the intersection, which melts and burns the solid fuel. The primary performance factor of combustion is the regression rate, which is a measure of the mixing of solid grain fuel with oxidizer. Therefore, a high quantity of heat flow within flame zone results in a high regression rate. The design of a basic HRM is depicted in Figure 12 (DeLuca, Lavagna, Maggi, Tadini, Pardini, Anselmo & Viola, 2014)..

6.2 Oxidizer

The oxidizer selection depends on numerous factors like specific impulse, regression rate, stability, density, and cost etc. As oxidizers, we can use Halogens (F_2, Cl_2, Br_2), but they are sensitive and toxic nature in nature are the major points of concern. For example, F_2O can be an effective selection because it gives a high specific impulse and also lighter in weight. However, it has some drawbacks as it is toxic, unstable, and also corrosive in nature. Moreover, it is also expensive, that's why it is not considered as a potential candidate of oxidizer for this mission design. Liquid oxygen (LOX) can also be seen as an oxidizer candidate because of its high specific impulse. The main disadvantages of LOX oxidizer are high cost, cryogenic nature, and lack of self-pressurizing property. On the other hand, Nitrous Oxide (N_2O) is the best and amply utilized oxidizer, which is readily available, self-pressurizing compound and produces a positive heat of formation. If we talk about its physical properties, its has density of 1.22g/ml, boiling point of $-88.5\,\text{C}^\text{o}$ and melting point $-90.8\,\text{C}^\text{o}$ (Zakirov, Wan, Shan, Zhang & Li, 2006). It goes through following reaction:

$$\text{N}_2\text{O} \rightarrow \text{N}_2 + \frac{1}{2}\text{O}_2 + 19.61\text{kcal/mol} \quad (22)$$

6.3 Fuel

There are numerous options which can be taken into consideration for a fuel of this system. If we consider some properties as a deciding factor, the best fuel is stable and provides high value of specific impulse along with high regression rate. The excessively used hybrid solid fuel is Hydroxyl Terminated Polybutadiene (HTPB). Its density is 0.9494g/ml, but when polymerized with Isonate (catalyst), the value of density beccomes $0.9651\ \text{g/ml}$. This is because the process of polymerization causes it to become stiffer, harder and stronger. The main advantage of using HTBP over other fuels is its stability and low cost. Meanwhile, there is also a disadvantage of HTPB that it has a low regression rate (Chluda, 2006).

6.4 Oxidizer injection

The regression is influenced by the factor of oxidizer flow rate. This is due to its dependence on the connective heat output from the flame to the grain of fuel. This regression rate can be increased by swirl injection due to swirl velocity component. A recirculation zone is formed in swirl flow and products preheat the combustible mixture in front of the flame combustion and therefore acts as a source

Table 4 Specifications of proposed HRM components.

Component		**Density, g/ml**
HRM Oxidizer	Nitrous Oxide (N_2O)	1.22
HRM Fuel	Hydroxyl Terminated Polybutadiene (HTPB)	0.9494
Oxidizer Injection	Swirl flow	N/A

of ignition to incoming mixture. This process is crucial because the flow of swirl actually regulates the combustion.

The flow of Swirl is categorized into two types of flow structures / components, rotational velocity and axial velocity components. The rotational velocity component is directed near surface and axial velocity components is directed along center. In the case of short grain, the average value of regression rate highly depends on the injection of swirl. The centrifugal force of flow of the oxidizer results in an optimum better regression rate of the fuel. We can determine the relation between regression rate and restrained parameters. The average value of regression rate is provided by the following mathematical equation (Chluda, 2006):

$$\dot{r}_{avg} = a_o \overline{G}_{ox}^{n} \quad (23)$$

In the above equation, $\dot{r}_o$ denotes average rate of regression, a_o determines experimental coefficient (grain length is included) of regression rate, $\overline{G}_{ox}$ represents average mass flux rate of the oxidizer and n denotes the exponent of regression rate.

7. Conclusion

Numerical modeling technique of the debris fragmentation has been analyzed with the help of real-time case studies of Cosmos 2251, Iridium 33 and Fengyun-1C collisions and NOVAA 16 explosion. Meanwhile HCS based ADR method has been proposed in this paper, which is not only feasible for removal of fragments but also a cost-effective solution for long-term operations. Furthermore, the orbits of aforementioned debris fragments are propagated in dynamic simulator which suggests that the critical regions with debris cluster in terms of orbital parameters (semi-major axis and inclination) are 1000 km and 82º, 800 km and 98º, 850 km and 71º respectively. We need to select an appropriate region where fragments are present in clusters that can be eliminated with a single operation attempt. An ADR technique is based on HRM based servicing platform that is composed of HCS, sensors and cameras to detect and identify cluster. After identification/detention it would be capable of capturing and de-orbiting a debris cluster in an effective manner. There are numerous aspects that can influence the mission design performance such as atmospheric drag, relative orbital speeds of system and the cluster. Furthermore, the design, oxidizer and fuel selection of HRM has also been discussed for this ADS mission.

8. Statements and Declarations

Acknowledgement: The authors wish to thank University of Luxembourg, Luxembourg and University of the Punjab, Lahore for providing the technical assistance to conduct the simulation analysis.

Conflict of Interest: The authors declare that they have no financial or personal relationships that could have inappropriately influenced the work reported in this paper

References

Air Command and Staff Coll Maxwell AFB al. (2009). AU-18 Space Primer.

Bess, T. D. (1975). *Mass distribution of orbiting man-made space debris* (No. L-10477).

Canadian Astronomy, Satellite Tracking and Optical Research (CASTOR), (2021) http://www.castor2.ca/03_Mechanics/03

TLE/B_Star.html

Carmicino, C., & Sorge, A. R. (2007). Performance comparison between two different injector configurations in a hybrid rocket. *Aerospace Science and Technology*, *11*(1), 61-67.

CelesTrack, (2020) https://celestrak.com/

Chluda, H. L. (2006). *Regression rate study of HTPB/nitrous oxide hybrid rockets* (Doctoral dissertation, University of Colorado at Boulder).

DeLuca, L. T., Lavagna, M., Maggi, F., Tadini, P., Pardini, C., Anselmo, L., ... & Viola, N. (2014). Large debris removal mission in LEO based on hybrid propulsion. *Aerotecnica Missili & Spazio*, *93*(1), 51-58.

Deshpande, S. P., Green, S. F., & Zarnecki, J. C. (1993). Size dependent space debris density distribution and implications for size to mass conversion. *Advances in Space Research*, *13*(8), 149-152.

ESA'S Annual Space Environment Report (2022), Space_Environment_Report_I6R0_20220422.pdf (esa.int)

Hakima, H., Bazzocchi, M. C., & Almstrom, B. (2022, March). Analysis of Satellite Drag Coefficients Based on Physical and Orbital Specifications. In *2022 IEEE Aerospace Conference (AERO)* (pp. 1-11). IEEE.

Hamilton, J., Blackwell, C., McSheehy, R., Juarez, Q., & Anz-Meador, P. (2017, April). Radar Measurements of Small Debris from HUSIR and HAX. In *European Conference on Space Debris* (No. JSC-CN-39228).

Hoots, F. R., & Roehrich, R. L. (1980). *Models for propagation of NORAD element sets*. Aerospace Defense Command Peterson AFB CO Office of Astrodynamics.

Johnson, N. L., Krisko, P. H., Liou, J. C., & Anz-Meador, P. D. (2001). NASA's new breakup model of EVOLVE 4.0. *Advances in Space Research*, *28*(9), 1377-1384.

Klima, R., Bloembergen, D., Savani, R., Tuyls, K., Hennes, D., & Izzo, D. (2016). Space debris removal: A game theoretic analysis. *Games*, 7(3), 20.

Lemaître, A. (2019). Space Debris: From LEO to GEO. *Satellite Dynamics and Space Missions*, 115-157.

Lederer, S. M., Stansbery, E. G., Cowardin, H. M., Hickson, P., Pace, L. F., Abercromby, K. J., ... & Alliss, R. J. (2013). *The NASA meter class autonomous telescope: Ascension Island*. National Aeronautics and Space administration Houston TX Lyndon B Johnson Space Center.

Lim, M. X., & Greenside, H. (2016). The external magnetic field created by the superposition of identical parallel finite solenoids. *American Journal of Physics*, *84*(8), 606-615.

Liou, J. C. (2011). An active debris removal parametric study for LEO environment remediation. *Advances in space research*, *47*(11), 1865-1876.

Liou, J. C., & Johnson, N. L. (2009). Characterization of the cataloged Fengyun-1C fragments and their long-term effect on the LEO environment. *Advances in Space Research*, *43*(9), 1407-1415.

Liou, J. C. (2011). Engineering and technology challenges for active debris removal. In *4th European Conference for Aerospace Sciences* (No. JSC-CN-24113).

Pardini, C., & Anselmo, L. (2007, September). Evolution of the debris cloud generated by the Fengyun-1C fragmentation event. In *Proceedings of the 20th International Symposium on Space Flight Dynamics*.

Pardini, C., & Anselmo, L. (2011). Physical properties and long-term evolution of the debris clouds produced

by two catastrophic collisions in Earth orbit. *Advances in Space Research*, *48*(3), 557-569.

Patera, R. P., & Ailor, W. H. (1998). The realities of reentry disposal. *Advances in Astronautical Sciences*, *99*, 1059-1071.

Rezunkov, Y. A. (2013). Active space debris removal by using laser propulsion. *Progress in Propulsion Physics*, *4*, 803-819.

Silha, J., Schildknecht, T., Hinze, A., Utzmann, J., Wagner, A., Willemsen, P., ... & Flohrer, T. (2014). Capability of a space-based space surveillance system to detect and track objects in GEO, MEO and LEO orbits.

Sorge, M., Peterson, G., & McVey, J. (2017). Forensic Analysis of the on-orbit Debris Generation Events. *7th ECSD, volume OTR, 513*.

Space-Track.Org RCS Legend, (2323) https://www.space-track.org/documentation/loadLegendRCS,

Stansbery G. Orbital debris research in the United States. 2009 Jun 1

Stansbery, G. (2014). NASA's Orbital Debris Program Office: Briefing to the NASA Advisory Council. *NASA, www.nasa.gov/sites/default/files/files/OrbitalDebrisProgramOffice. pdf*.

Stottler, R. (2015). Improved Space Surveillance Network (SSN) Scheduling using Artificial Intelligence Techniques. *Ica AMOS 2015 Proceedings*.

Tan, A., Reynolds, R. C., & Schamschula, M. (2017). NOAA-16 Satellite Fragmentation in Orbit: Genesis of the Gabbard Diagram and Estimation of the Intensity of Breakup. *Adv. Aerospace Sci. Appl*, *7*, 37-47.

Wang, T. (2010). Analysis of Debris from the Collision of the Cosmos 2251 and the Iridium 33 Satellites. *Science & Global Security*, *18*(2), 87-118.

Zakirov, V., Wan, K., Shan, F. L., Zhang, H. Y., & Li, L. M. (2006). Restartable hybrid rocket motor using nitrous oxide. In *57th International Astronautical Congress* (pp. C4-2).